



Optical analysis of a III-V-nanowire-array-on-Si dual junction solar cell

YANG CHEN,^{1,*} OLIVER HÖHN,² NICO TUCHER,² MATS-ERIK PISTOL,¹ AND NICKLAS ANTTU¹

¹Division of Solid State Physics and NanoLund, Lund University, Box 118, 22100 Lund, Sweden

²Fraunhofer Institute for Solar Energy Systems ISE, Heidenhofstr. 2, 79110 Freiburg, Germany

*yang.chen@fif.lth.se

Abstract: A tandem solar cell consisting of a III-V nanowire subcell on top of a planar Si subcell is a promising candidate for next generation photovoltaics due to the potential for high efficiency. However, for success with such applications, the geometry of the system must be optimized for absorption of sunlight. Here, we consider this absorption through optics modeling. Similarly, as for a bulk dual-junction tandem system on a silicon bottom cell, a bandgap of approximately 1.7 eV is optimum for the nanowire top cell. First, we consider a simplified system of bare, uncoated III-V nanowires on the silicon substrate and optimize the absorption in the nanowires. We find that an optimum absorption in 2000 nm long nanowires is reached for a dense array of approximately 15 nanowires per square micrometer. However, when we coat such an array with a conformal indium tin oxide (ITO) top contact layer, a substantial absorption loss occurs in the ITO. This ITO could absorb 37% of the low energy photons intended for the silicon subcell. By moving to a design with a 50 nm thick, planarized ITO top layer, we can reduce this ITO absorption to 5%. However, such a planarized design introduces additional reflection losses. We show that these reflection losses can be reduced with a 100 nm thick SiO₂ anti-reflection coating on top of the ITO layer. When we at the same time include a Si₃N₄ layer with a thickness of 90 nm on the silicon surface between the nanowires, we can reduce the average reflection loss of the silicon cell from 17% to 4%. Finally, we show that different approximate models for the absorption in the silicon substrate can lead to a 15% variation in the estimated photocurrent density in the silicon subcell.

© 2017 Optical Society of America

OCIS codes: (040.5350) Photovoltaic; (310.6628) Subwavelength structures, nanostructures; (300.1030) Absorption; (350.4238) Nanophotonics and photonic crystals.

References and links

1. K. E. Martin, A. Green, Y. Hishikawa, W. Warta, E. D. Dunlop, D. H. Levi, and A. W. Y. Ho-Baillie, "Solar cell efficiency table (version 49)," *Prog. Photovoltaics* **25**, 3 (2017).
2. S. Essig, M. A. Steiner, C. Allebé, J. F. Geisz, B. Paviet-Salomon, S. Ward, A. Descoedres, V. LaSalvia, L. Barraud, N. Badel, A. Faes, J. Levrat, M. Despeisse, C. Ballif, P. Stradins, and D. L. Young, "Realization of GaInP/Si dual-junction solar cells with 29.8% 1-sun efficiency," *IEEE J. Photovolt.* **6**(4), 1012–1019 (2016).
3. G. Kastner and U. Gosele, "Stress and dislocations at cross-sectional heterojunctions in a cylindrical nanowire," *Philos. Mag.* **84**(35), 3803–3824 (2004).
4. M. Yao, S. Cong, S. Arab, N. Huang, M. L. Povinelli, S. B. Cronin, P. D. Dapkus, and C. Zhou, "Tandem solar cells using GaAs nanowires on Si: Design, fabrication, and observation of voltage addition," *Nano Lett.* **15**(11), 7217–7224 (2015).
5. J. Wallentin, N. Anttu, D. Asoli, M. Huffman, I. Aberg, M. H. Magnusson, G. Siefert, P. Fuss-Kailuweit, F. Dimroth, B. Witzigmann, H. Q. Xu, L. Samuelson, K. Deppert, and M. T. Borgström, "InP nanowire array solar cells achieving 13.8% efficiency by exceeding the ray optics limit," *Science* **339**(6123), 1057–1060 (2013).
6. I. Åberg, G. Vescovi, D. Asoli, U. Naseem, J. P. Gilboy, C. Sundvall, A. Dahlgren, K. E. Svensson, N. Anttu, M. T. Björk, and L. Samuelson, "A GaAs nanowire array solar cell with 15.3% efficiency at 1 sun," *IEEE J. Photovolt.* **6**(1), 185–190 (2016).
7. M. Yao, N. Huang, S. Cong, C.-Y. Chi, M. A. Seyedi, Y.-T. Lin, Y. Cao, M. L. Povinelli, P. D. Dapkus, and C. Zhou, "GaAs nanowire array solar cells with axial p-i-n junctions," *Nano Lett.* **14**(6), 3293–3303 (2014).
8. G. Mariani, A. C. Scofield, C. H. Hung, and D. L. Huffaker, "GaAs nanopillar-array solar cells employing in situ surface passivation," *Nat. Commun.* **4**, 1497 (2013).

9. Y. Cui, J. Wang, S. R. Plissard, A. Cavalli, T. T. Vu, R. P. van Veldhoven, L. Gao, M. Trainor, M. A. Verheijen, J. E. Haverkort, and E. P. Bakkers, "Efficiency enhancement of InP nanowire solar cells by surface cleaning," *Nano Lett.* **13**(9), 4113–4117 (2013).
10. H. Goto, K. Nosaki, K. Tomioka, S. Hara, K. Hiruma, J. Motohisa, and T. Fukui, "Growth of core-shell InP nanowires for photovoltaic application by selective-area metal organic vapor phase epitaxy," *Appl. Phys. Express* **2**, 035004 (2009).
11. J. A. Czaban, D. A. Thompson, and R. R. LaPierre, "GaAs core-shell nanowires for photovoltaic applications," *Nano Lett.* **9**(1), 148–154 (2009).
12. D. van Dam, N. J. van Hoof, Y. Cui, P. J. van Veldhoven, E. P. Bakkers, J. Gómez Rivas, and J. E. Haverkort, "High-efficiency nanowire solar cells with omnidirectionally enhanced absorption due to self-aligned indium-tin-oxide Mie scatterers," *ACS Nano* **10**(12), 11414–11419 (2016).
13. M. Borg, H. Schmid, K. E. Moselund, G. Signorello, L. Gignac, J. Bruley, C. Breslin, P. Das Kanungo, P. Werner, and H. Riel, "Vertical III-V nanowire device integration on Si(100)," *Nano Lett.* **14**(4), 1914–1920 (2014).
14. R. LaPierre, "Theoretical conversion efficiency of a two-junction III-V nanowire on Si solar cell," *J. Appl. Phys.* **110**(1), 014310 (2011).
15. N. Huang, C. Lin, and M. L. Povinelli, "Limiting efficiencies of tandem solar cells consisting of III-V nanowire arrays on silicon," *J. Appl. Phys.* **112**(6), 064321 (2012).
16. Y. Hu, M. Li, J. J. He, and R. R. LaPierre, "Current matching and efficiency optimization in a two-junction nanowire-on-silicon solar cell," *Nanotechnology* **24**(6), 065402 (2013).
17. Y. Wang, Y. Zhang, D. Zhang, S. He, and X. Li, "Design high-efficiency III-V nanowire/Si two-junction solar cell," *Nanoscale Res. Lett.* **10**(1), 269 (2015).
18. A. Benali, J. Michallon, P. Regreny, E. Drouard, P. Rojo, N. Chauvin, D. Bucci, A. Fave, A. Kaminski-Cachopo, and M. Gendry, "Optical simulation of multijunction solar cells based on III-V nanowires on silicon," *Energy Procedia* **60**, 109–115 (2014).
19. A. P. Foster and L. R. Wilson, "Design parameters for nanowire-planar tandem solar cells," *Phys. Status Solidi* **210**(2), 425–429 (2013).
20. S. Bu, X. Li, L. Wen, X. Zeng, Y. Zhao, W. Wang, and Y. Wang, "Optical and electrical simulations of two-junction III-V nanowires on Si solar cell," *Appl. Phys. Lett.* **102**(3), 031106 (2013).
21. X. Li, T. Shi, G. Liu, L. Wen, B. Zhou, and Y. Wang, "Absorption enhancement of GaInP nanowires by tailoring transparent shell thicknesses and its application in III-V nanowire/Si film two-junction solar cells," *Opt. Express* **23**(19), 25316–25328 (2015).
22. Y. Chen, M. E. Pistol, and N. Anttu, "Design for strong absorption in a nanowire array tandem solar cell," *Sci. Rep.* **6**(1), 32349 (2016).
23. N. Tucher, J. Eisenlohr, P. Kiefel, O. Höhn, H. Hauser, M. Peters, C. Müller, J. C. Goldschmidt, and B. Bläsi, "3D optical simulation formalism OPTOS for textured silicon solar cells," *Opt. Express* **23**(24), A1720–A1734 (2015).
24. N. Anttu and H. Xu, "Scattering matrix method for optical excitation of surface plasmons in metal films with periodic arrays of subwavelength holes," *Phys. Rev. B* **83**(16), 165431 (2011).
25. A. De Vos, "Detailed balance limit of the efficiency of tandem solar cells," *J. Phys. D Appl. Phys.* **13**(5), 839–846 (1980).
26. W. Shockley and H. J. Queisser, "Detailed balance limit of efficiency of p-n junction solar cells," *J. Appl. Phys.* **32**(3), 510–519 (1961).
27. C. A. Gueymard, D. Myers, and K. Emery, "Proposed reference irradiance spectra for solar energy systems testing," *Sol. Energy* **73**(6), 443–467 (2002).
28. M. A. Green, K. Emery, Y. Hishikawa, W. Warta, and E. D. Dunlop, "Solar cell efficiency tables (version 48)," *Prog. Photovolt. Res. Appl.* **24**(7), 905–913 (2016).
29. I. Vurgaftman, J. Meyer, and L. Ram-Mohan, "Band parameters for III-V compound semiconductors and their alloys," *J. Appl. Phys.* **89**(11), 5815–5875 (2001).
30. E. D. Palik, *Handbook of Optical Constants of Solids* (Academic Press, 1998), Vol. 3.
31. K. Masuko, M. Shigematsu, T. Hashiguchi, D. Fujishima, M. Kai, N. Yoshimura, T. Yamaguchi, Y. Ichihashi, T. Mishima, N. Matsubara, T. Yamanishi, T. Takahama, M. Taguchi, E. Maruyama, and S. Okamoto, "Achievement of more than 25% conversion efficiency with crystalline silicon heterojunction solar cell," *IEEE J. Photovolt.* **4**(6), 1433–1435 (2014).
32. M. A. Green, "Solar cells: operating principles, technology, and system applications," (1982).
33. F. Abelès, "VI methods for determining optical parameters of thin films," *Prog. Opt.* **2**, 249–288 (1963).
34. S. Divitt and L. Novotny, "Spatial coherence of sunlight and its implications for light management in photovoltaics," *Optica* **2**(2), 95–103 (2015).
35. B. Wang and P. W. Leu, "Tunable and selective resonant absorption in vertical nanowires," *Opt. Lett.* **37**(18), 3756–3758 (2012).
36. N. Anttu and H. Q. Xu, "Efficient light management in vertical nanowire arrays for photovoltaics," *Opt. Express* **21**(S3 Suppl 3), A558–A575 (2013).
37. H. J. Joyce, J. Wong-Leung, C.-K. Yong, C. J. Docherty, S. Paiman, Q. Gao, H. H. Tan, C. Jagadish, J. Lloyd-Hughes, L. M. Herz, and M. B. Johnston, "Ultralow surface recombination velocity in InP nanowires probed by terahertz spectroscopy," *Nano Lett.* **12**(10), 5325–5330 (2012).

1. Introduction

Silicon is presently the dominating material for the photovoltaics market, and an efficiency of 26.3% has been achieved with a single junction crystalline silicon cell [1]. To enhance the efficiency, a tandem design with a GaInP subcell on top of a Si subcell has reached an efficiency of 30.5% [1,2].

Compared to planar layers, nanowires offer the possibility of direct, monolithic fabrication of III-V semiconductors on silicon, despite possible lattice mismatch [3]. Recently, an efficiency of 11.4% was demonstrated in a tandem cell consisting of a GaAs nanowire-array subcell grown epitaxially on top of a silicon subcell [4]. In addition, the efficiency of single-junction III-V nanowire array solar cells has shown rapid increase [5–11], with current record efficiencies of 13.8% and 15.3% for epitaxially grown InP and GaAs nanowire arrays [5,6], and 17.8% for top-down fabricated InP nanowire arrays [12]. Thus, there is prospect for future applications with III-V-nanowire-array-on-silicon tandem solar cells, and such nanowire array on silicon structure can be achieved, by selective area growth, even on industry-standard silicon (100) substrates [13].

The nanowire-array-on-silicon tandem cell has attracted much interest also from the modeling side [14–21]. First, the emphasis was on the electrical aspects of the tandem cell [14], and the absorption in the nanowires was approximated with that in a bulk layer. Later, the diffraction of light was included in the optics analysis [15–21]. Then, it was shown that the photocurrent density in the nanowire subcell and the silicon subcell can be optimized and matched by tuning the diameter of the nanowires and the pitch of the nanowire array [15–21]. However, typically a significant reflection of about 20%-30% shows up in the wavelength region between the bandgap of the nanowires and the bandgap of the silicon [20,21]. Furthermore, in these previous optics studies, the focus was on a bare nanowire array [15–20] or on a bare nanowire array with a dielectric shell [21], and the effect of additional processing layers was not considered. Thus, there exists a need for a dedicated study of light-management in a nanowire-array-on-silicon design, which includes the effect of processing and anti-reflection layers.

In this work, we study through electromagnetic modeling the optical response of a III-V-nanowire-array-on-Si dual junction solar cell. First, we optimize the geometry of the nanowires for absorption in the nanowire array. Then, we discuss the impact of varying configurations of an indium tin oxide (ITO) top contact layer on the optical response. We show that a conformal ITO layer can absorb 37% of the low energy photons intended for absorption in the silicon subcell. By moving to a 50 nm planarized contacting scheme, this absorption loss in the ITO can be reduced by 86%.

Note that we consider the specific case of a planar silicon cell underneath the nanowire array together with the planar ITO contact design. In this case, the reflection problem for this nanowire array on silicon tandem system is different from single junction nanowire array solar cells [5] and nanowire arrays with a dual junction in the nanowires themselves [22]. We show that an anti-reflection coating (ARC) design with one ARC at the top of the nanowire layer and one ARC on top of the silicon surface can reduce this reflection loss by 77%.

We analyze also the impact of varying models for the absorption in the silicon subcell. In one model, we assume that the silicon subcell is infinitely thick. In this case, all the incident above-bandgap photons that can couple into the silicon cell will be absorbed. In another model, we assume that the silicon cell is 300 μm thick and that light propagates only once through it without additional scattering back into the silicon cell. Thus, we assume a single-pass absorption as described by the Beer-Lambert law. These two models, which describe maximum and minimum light-trapping, lead to a 15% difference in the estimated photocurrent density in the silicon subcell. Finally, we include the light-trapping caused by the scattering of light from the nanowire array at the top side and a diffraction grating at the bottom side with the help of OPTOS [23]. As expected, the results from this rigorous

modeling fall between the results of the two extreme cases above. Our optics study is a natural starting point for future full opto-electronic studies.

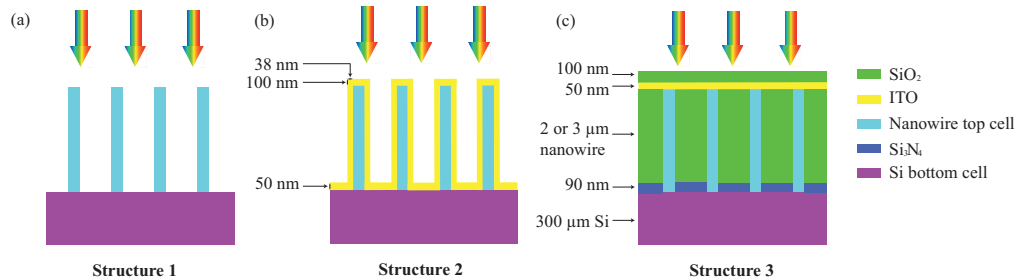


Fig. 1. Schematics of a nanowire array on a silicon substrate. (a) Bare nanowire array. (b) Nanowire array with conformal ITO layer. (c) Nanowire array with planarized ITO layer together with a top and a bottom ARC.

2. Device structure

We consider three different configurations for a square array of III-V nanowires on top of a silicon substrate as shown in Fig. 1. There are three geometry parameters in such a nanowire array: the diameter D of the nanowires, the length L of the nanowires, and the pitch P of the square array, which is the distance between the centers of neighboring nanowires. Structure 1 in Fig. 1(a) is a system with a bare nanowire array, which is the geometrically simplest system to start with. For Structure 2 in Fig. 1(b), we have included a conformal ITO top contact over the nanowires and the substrate. In Structure 3, we consider a planar ITO top contact with a SiO_2 layer of refractive index $n \sim 1.5$ between the nanowires to planarize the array. Note that the results with such a SiO_2 layer are applicable also for other $n \sim 1.5$ materials, such as polymers, which are often used for planarizing nanowire array cells [7]. Furthermore, in Structure 3, we use an anti-reflection coating (ARC) of SiO_2 on top of the ITO and a second ARC of Si_3N_4 on the substrate surface between the nanowires.

3. Method for modeling the optical response of nanowire arrays

We model the optical response of the nanowire array with the Maxwell equations [24]. In this way, we include the diffraction and interference of light due to the three-dimensional geometry of the nanowires and the processing layers around the nanowires. The optical response of the constituent materials is included through the wavelength dependent refractive index $n(\lambda)$ of each material. From this modeling, we extract the reflectance $R(\lambda)$ of the system, the transmittance $T(\lambda)$ into the silicon substrate, and the absorptance $A_{\text{NW}}(\lambda)$ and $A_{\text{ITO}}(\lambda)$ of the nanowires and the ITO, respectively. Note that $R(\lambda)$, $T(\lambda)$, and $A(\lambda)$ denote the fraction of incident light at wavelength λ that is reflected, transmitted, or absorbed.

We used for the modeling alternatively the scattering matrix method [24] and the finite element method (through Comsol Multiphysics). For example, for Structures 1 and 3, the scattering matrix method was preferred due to computational speed. But to discriminate spatially between the absorption in the radial direction between the nanowire and the radial ITO shell in Structure 2, the finite element method was faster. Both methods solve the same Maxwell equations, and we ascertained that they give equivalent results, enabling us to interchangeably use whichever method was most convenient.

Unless explicitly stated otherwise, we assume a semi-infinite silicon substrate that can absorb all of the above bandgap light that enters it. In that case, the absorption in the silicon substrate is given by $A_{\text{Si}}(\lambda) = T(\lambda)$ for $\lambda < \lambda_{\text{bg,Si}}$ where $\lambda_{\text{bg,Si}} = hc/E_{\text{bg,Si}} = 1107 \text{ nm}$ with $E_{\text{bg,Si}} = 1.12 \text{ eV}$ the bandgap energy of silicon, h the Planck constant, and c the speed of light in vacuum. Note that we discuss possible below-bandgap contribution to the photocurrent density in Section 9.

4. Choice for nanowire material

The bandgap of the nanowire material affects the wavelength range from which the nanowires can absorb light, setting an upper limit on the photocurrent density in the nanowire-array subcell. Similarly, the nanowire bandgap affects how much of the incident light that can reach the silicon substrate without being absorbed in the nanowires, limiting the photocurrent density in the silicon cell. In this work, for the choice of the nanowire material, we assumed a monolithically connected 2-terminal tandem cell. In such a tandem cell, we have a requirement on current matching between the top and the bottom cell: The current in the tandem cell is set by the subcell that shows the lowest current [25]. For this case, the Shockley-Queisser detailed balance analysis [26] yields an optimum bandgap of 1.74 eV for the nanowires under the AM1.5G spectrum [27], when assuming perfect absorption of above bandgap photons in both the nanowire array and in the silicon. When we instead consider experimentally measured external quantum efficiency of nanowire solar cells and silicon cells [5,6,28], we estimate that a slightly lower nanowire bandgap of 1.64 eV gives a better current matching. Therefore, in this work, we investigate three different bandgaps of $E_{\text{bg,NW}} = 1.64$, 1.7 and 1.74 eV for the nanowire top cell. We chose to consider $\text{Ga}_x\text{In}_{1-x}\text{P}$ and $\text{GaAs}_x\text{P}_{1-x}$ for the nanowires, which cover this bandgap range [29]. For $n(\lambda)$ for these ternaries, we used an interpolation from tabulated data for GaAs, InP and GaP [30].

5. Optimization of the geometry of the nanowire array

We performed an optimization of the geometry of the nanowires in Structure 1 and Structure 3 (see Fig. 1 for schematics of the structures) in terms of the photocurrent density j_{NWs} of the nanowires. Specifically, we assumed that each absorbed photon with energy above the bandgap gives rise to an electron-hole pair that contributes to the photocurrent density:

$$j_{\text{NWs}} = \frac{e}{hc} \int_{\lambda_{\text{start}}}^{\lambda_{\text{bg,NWs}}} \lambda I_{\text{AM1.5G}} A_{\text{NWs}}(\lambda) d\lambda \quad (1)$$

Here, $I_{\text{AM1.5G}}$ is the incident intensity of the AM1.5G solar spectrum [27], $\lambda_{\text{start}} = 280$ nm is the wavelength below which the AM1.5G spectrum shows negligible intensity, and $\lambda_{\text{bg,NW}} = hc/E_{\text{bg,NW}}$ is the bandgap wavelength of the nanowires.

We consider nanowires of a length of either 2 or 3 μm , which have been used for single-junction nanowire array solar cells to reach strong absorption [5,6]. In the optimization of the remaining geometry parameters, we allowed for a variation of the nanowire diameter D and the array pitch P , with the nanowires placed in a square array. For the planarized Structure 3, we fill in between the nanowire with $n \sim 1.5$ material. Regarding the Si_3N_4 ARC layer in Structure 3, the absorptance in the nanowires is almost independent of the thickness of the Si_3N_4 layer (see Appendix A). As a result, the thickness of the Si_3N_4 layer does not affect noticeably the optimized values of the other parameters. We studied this Si_3N_4 thickness as an independent parameter and optimized this layer according to the reflection of the tandem solar cell. Similarly, we considered the thickness of the SiO_2 ARC layer on the top side as an independent parameter in the optimization. In the optimization of Structure 3, we used a fixed thickness of 100 nm and 90 nm for the SiO_2 and the Si_3N_4 ARC layers, respectively, and a thickness of 50 nm for the ITO top contact layer. More details of the optimization can be found in Appendix B and in [22]. The resulting optimized diameter and pitch are given in Table 1 and Table 2 of Appendix B for varying material, and consecutively bandgap, of the nanowires. For example, we find optimized absorption for a nanowire diameter in the range of 100-200 nm, depending on the nanowire length and material. For such an optimized diameter, the optimum pitch corresponds to approximately 16 nanowires per square micrometer.

In this work, to enable easier analysis and discussion of varying reflection, transmission, and absorption processes, we translated the corresponding spectrum to an equivalent photocurrent density:

$$j_x = \frac{e}{hc} \int_{\lambda_{X,start}}^{\lambda_{X,end}} \lambda I_{AM1.5G} X(\lambda) d\lambda \quad (2)$$

For $X(\lambda) = T(\lambda)$ in Eq. (2), that is, for $j_X = j_T$, we considered the silicon cell and used $\lambda_{X,start} = 280$ nm and $\lambda_{X,end} = \lambda_{bg,Si} = 1107$ nm. For $X(\lambda) = A_{ITO}(\lambda)$, that is, for $j_X = j_{ITO}$, and for $X(\lambda) = R(\lambda)$, that is, for $j_X = j_R$, we considered the loss of photons that could have been absorbed in the dual junction cell, either in the nanowire or the silicon subcell, and used therefore $\lambda_{X,start} = 280$ nm and $\lambda_{X,end} = \lambda_{bg,Si}$. In the last column of Tables 1 and 2, we show also values for $X(\lambda) = R(\lambda)$ for $\lambda_{X,start} = \lambda_{bg,NWs}$ and $\lambda_{X,end} = \lambda_{bg,Si}$, which is the reflection loss of photons dedicated exclusively for absorption in the silicon cell.

In Table 1 and Table 2, we show the geometry parameters that optimize j_{NWs} for the bandgap of 1.64, 1.70, and 1.74 eV for the nanowire material. For most designs, j_{NWs} is larger than j_T , the photocurrent density in the silicon subcell as calculated from the transmission spectrum of light entering the silicon substrate. A design with $j_{NWs} > j_T$ can be motivated by the fact that nanowire array cells have shown a lower EQE relative to that of silicon cells, as mentioned in Section 4 [6,31]. In the optimization tables (Table 1 and Table 2), bare nanowires with air between the nanowires show an optimized diameter of 140 nm. In [22] we discussed that the product of E_g , the bandgap energy, n_g , the refractive index in the vicinity of the bandgap, and D_{res} , the resonance diameter that optimizes broadband absorption, is a constant. For InP, the resonance diameter of the HE11 mode is 180 nm, with $n_g = 3.5$ and $E_g = 1.34$ eV. From these values, we can calculate the expected optimum diameter for the nanowire array with a bandgap of 1.7 eV to be 140 nm. However, when we consider here the array where SiO₂ planarizes the space between the nanowires, this diameter shifts to 170 nm, as seen in Table 2. The reason for this shift can be assigned to the smaller refractive index difference in nanowire/SiO₂ system than in nanowire/air system. The smaller difference makes the optical resonance weaker and the HE11 resonance diameter shifts to a higher value.

6. Benefit of a planar ITO over a conformal ITO for optimized geometry

In this section, we show a practical merit of Structure 3 compared to Structure 1. We start with Structure 1 and proceed, through Structure 2, to Structure 3 (see Fig. 1 for a schematic). For this demonstration, we focus on the 1.7 eV bandgap GaInP nanowire array with 2000 nm long nanowires. For Structures 1 and 2, we used a diameter of 140 nm and a pitch of 260 nm (as for the optimized geometry of Structure 1, which is marked by * in Table 1). For Structure 3, we used a diameter of 170 nm and a pitch of 240 nm (as for the optimized geometry of Structure 3, which is marked by * in Table 2). This optimized geometry gives an upper bound of 21.3 mA/cm² to the current density.

First, to make Structure 1 more realistic for solar cell applications, we include an ITO top contact layer. In the modeling, we used the values for the refractive index of ITO given in the Supplementary Material of [5]. We start by considering a conformally coated ITO layer, which leads us to Structure 2 in Fig. 1(b). Note that in experiments, such a conformal ITO layer requires an insulating layer like SiO₂ [5]. However, here, for simplicity, we directly coat the nanowires with ITO in the form of a 38 nm thick radial shell, a 100 nm thick layer at the top of the nanowires, and a 50 nm thick layer on top of the substrate. These thicknesses were inspired by experiments [5]. However, we should note that, due to the much smaller pitch-to-diameter ratio in our optimization compared to experiments [5], the conformal coating in

Structure 2 leads to a quite large volume of ITO. Actually, the volume of ITO corresponds to a 700 nm thick planar layer, and 90% of this ITO is on the sidewalls of the nanowires.

Such a large volume of ITO results in an ITO absorption which is on average 37% in the wavelength range between the nanowire bandgap and the silicon bandgap as shown in Fig. 2(a). The absorption loss in the ITO corresponds to a loss of $j_{\text{ITO}} = 9.4 \text{ mA/cm}^2$ in the photocurrent density, as calculated from Eq. (2). We note that this ITO absorption loss can be reduced to $j_{\text{ITO}} = 4.7 \text{ mA/cm}^2$ by moving to a larger nanowire diameter (see Fig. 7 in Appendix C).

Alternatively, by moving to a design with a planarized ITO top contact, j_{ITO} can be further reduced. We show in Fig. 2(b) the spectrum for the optimized nanowire array diameter, pitch and length in Structure 3 with a planar ITO of 50 nm in thickness. The absorption loss in the ITO corresponds to $j_{\text{ITO}} = 1.3 \text{ mA/cm}^2$ as shown in Fig. 2(b). Thus, we can decrease the absorption in the ITO, in terms of j_{ITO} , by 86% by moving from the conformal ITO coating to the 50 nm thick planar ITO layer.

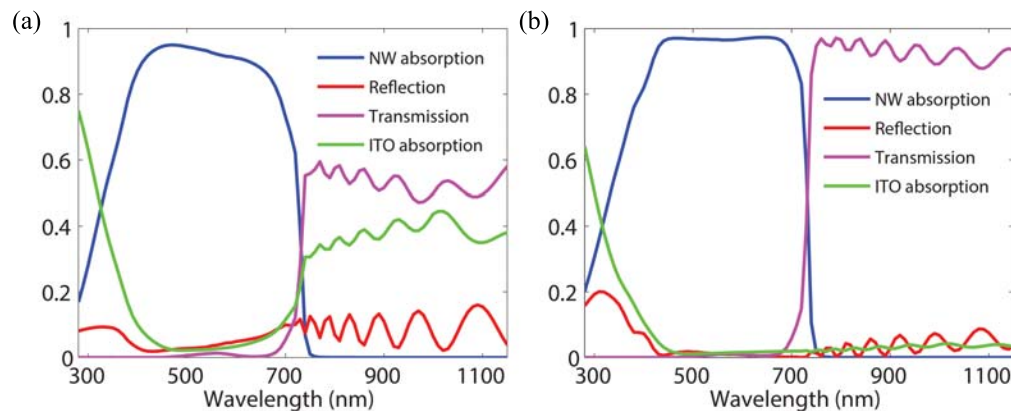


Fig. 2. Optical response of (a) Structure 2 and (b) Structure 3 as for the optimized system marked by (*) in Table 1 and Table 2, respectively. The ITO absorption in (a) corresponds to a photocurrent density of 9.4 mA/cm^2 through Eq. (2).

7. Effect of thickness of planar ITO layer

Next, we consider the absorption loss in the planar ITO of Structure 3 as a function of ITO thickness as shown in Fig. 3(a). First, for a thin ITO layer, with increasing thickness, the absorption in the ITO increases and the reflection of the system decreases. We assign this increased ITO absorption to the increasing volume of absorbing ITO. The reduced reflection we assign in turn to the ITO layer acting as a partially absorbing ARC. Interestingly, the nanowire absorption and the transmission to the silicon substrate are kept almost constant up to an ITO thickness of 50 nm. Thus, here, the increasing anti-reflection effect of the ITO layer compensates for the increasing absorption loss in the ITO. Therefore, from the optical point of view, an ITO thickness up to 50 nm is preferable.

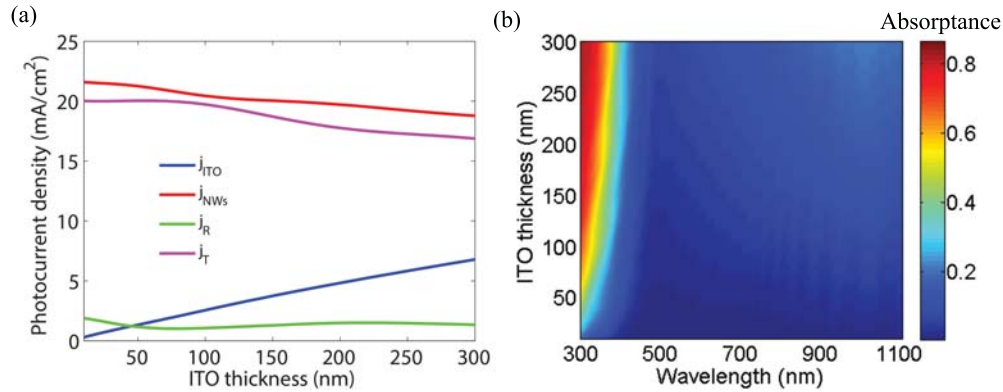


Fig. 3. (a) Absorption in the nanowires and in the ITO, reflection loss, and transmission into the silicon substrate for varying ITO thickness in Structure 3 marked by (*) in Table 2. Note that these results are translated into equivalent photocurrent density values through Eq. (1) and Eq. (2). (b) ITO absorptance $A_{\text{ITO}}(\lambda)$ for the varying ITO thicknesses considered in (a).

However, in an actual solar cell, resistive electrical losses occur in the ITO layer, and these decrease with a thicker, more conductive ITO layer. To reduce the resistive losses in the ITO layer, metallic contact fingers can be used for spreading the current. However, such contact fingers shadow part of the solar cell. The combined optimization of ITO layer thickness, absorption loss in the ITO layer, and contact finger design is beyond the scope of the present work. However, we can state that for the 50 nm thick ITO, which is the thickness recommended from the above optics modeling, we expect a resistive loss of approximately 1% with a contact finger separation of 4.7mm. This loss was calculated with Eq. (8.23) from [32] assuming a sheet resistance of 50 ohms square, which can be reached in a 50 nm thick ITO layer [5].

In Fig. 3(b), the absorption spectrum of the ITO layer as a function of ITO thickness is shown. When the ITO thickness is above 100 nm, the ITO absorptance $A_{\text{ITO}}(\lambda)$ shows a high value of above 80% for $\lambda < 300$ nm. However, the incident photon flux of the AM1.5G spectrum is almost negligible in this wavelength region. With 50 nm and 100 nm ITO thickness, the average ITO absorption for $\lambda_{\text{bg,NWs}} < \lambda < \lambda_{\text{bg,Si}}$ is less than 5% and 10%, respectively.

8. Benefit of single-layer ARC

Above, we discussed the effect of the absorption loss in the ITO layer. Reflection is another loss mechanism that reduces the photocurrent-density potential of the nanowire-array-on-silicon tandem cell. For example, the bare nanowire array of Structure 1 shows a 10-30% reflectance for $\lambda_{\text{bg,NWs}} < \lambda < \lambda_{\text{bg,Si}}$, red line in Fig. 4(a). In this case, the reflection loss corresponds to a photocurrent density of $j_{\text{R}} = 4.7$ mA/cm² through Eq. (2). Actually, if we fill the space between the nanowires with SiO₂ and add a planar ITO layer, that is, when we consider Structure 3 but without the SiO₂ and Si₃N₄ ARC layers, the reflection loss increases to $j_{\text{R}} = 5.8$ mA/cm², see dashed red line in Fig. 4(b) for the corresponding reflection spectrum. Thus, there is a clear need for ARC layers in Structure 3. We note that for normally incident light of a single wavelength λ , we can suppress with a single-layer ARC the reflection to zero for a system consisting of a single interface between materials of refractive index n_1 and n_2 . For this case, the optimized ARC has a refractive index of $n_{\text{ARC}} = (n_1 n_2)^{1/2}$ and a thickness of $t_{\text{ARC}} = \lambda / (4n_{\text{ARC}})$ [33].

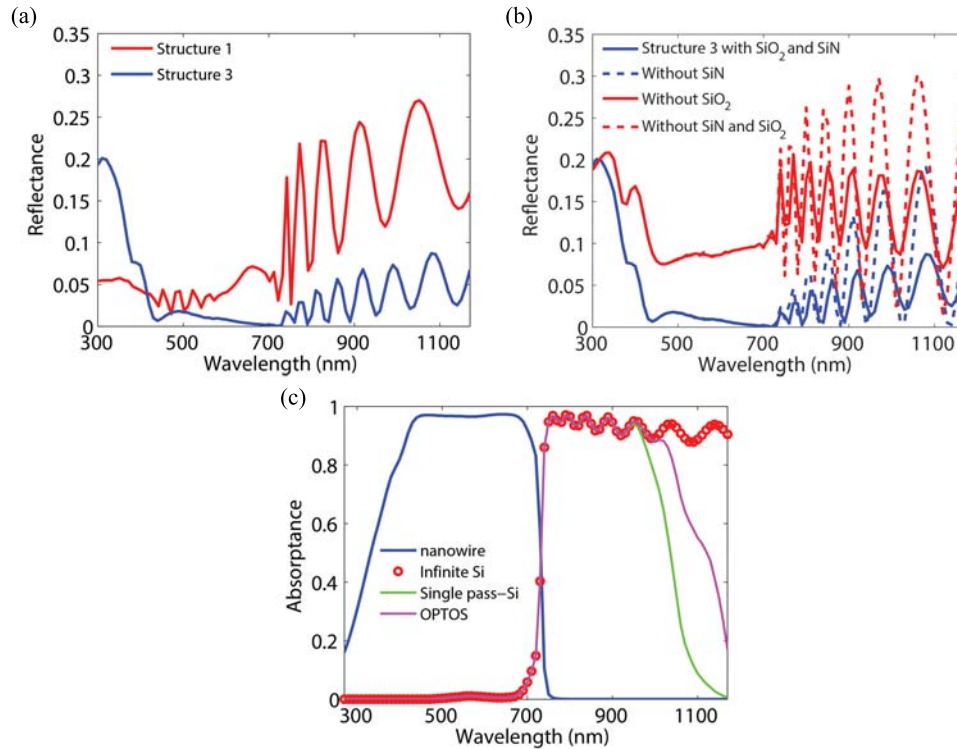


Fig. 4. (a) Reflection of Structure 1 and 3 with optimized diameter and pitch (as marked by (*) in Table 1 and Table 2, respectively). (b) Reflection of Structure 3 with varying configuration of the ARC layers. (c) Absorption in the nanowire array and the silicon substrate in Structure 3 of (a). We show here results for three different assumptions for the absorption in the silicon.

To reduce the reflection loss of the tandem solar cell, we aimed to reduce the reflection by moving to Structure 3 from Structure 1. Two ARC layers are used. The top (bottom) ARC layer is designed to reduce the reflection of above bandgap photons in the nanowire array (silicon substrate). We optimized the ARCs for the wavelengths of 600 nm and 1000 nm, respectively. At these two wavelengths, Structure 1 shows in Fig. 4(a) the highest reflection above the nanowire material bandgap and between nanowire material and silicon bandgaps, respectively. This rough estimate agrees with the spectrum-weighted reflection study of ARC thickness as shown in Appendix A.

At this wavelength of $\lambda \approx 600$ nm, ITO has a refractive index of 2.0, which asks for $n_{\text{ARC}} = 1.41$, reasonably close to the $n = 1.46$ of SiO_2 at $\lambda = 600$ nm. Therefore, we chose SiO_2 for the top ARC material, and we used $t_{\text{ARC}} = 100$ nm (as approximated from $n_{\text{ARC}} \approx 1.5$). Note that we used this 100 nm thickness throughout the optimization leading to the values in Table 2.

In contrast, for the interface into the silicon substrate, we chose to minimize the reflection for $\lambda = 1000$ nm in order to optimize the transmission of the long wavelength light, which is not absorbed in the nanowires. Note that we chose to use SiO_2 to fill the space between the nanowires, and Si_3N_4 can be used as a growth mask on top of the silicon surface [4]. Actually, the Si_3N_4 has a refractive index of 2.0 at 1000 nm, which is a good match for an ARC material for an interface between SiO_2 and silicon. From the above discussion, we would use $t_{\text{ARC}} = 125$ nm for a planar Si_3N_4 ARC at $\lambda = 1000$ nm. However, note that the ARC layer does not entirely consist of Si_3N_4 due to the nanowires. We studied the thickness dependence of spectrum-weighted reflection in Appendix A. The estimation from a simple linear effective refractive index equation agrees with the parameter sweep study very well. The linear equation can be written as $n_{\text{eff}} = (1-x)n_{\text{SiN}} + x \cdot n_{\text{NW}}$. Here, $x = \pi(D/2)^2/P^2$ is the area coverage

of nanowires in the array. For the considered nanowire array of $D = 170$ nm and $P = 240$ nm (marked by * in Table 2), we find $x = 0.39$. With $n_{\text{NW}} \approx 3.5$ at $\lambda = 1000$ nm, we would expect that a Si_3N_4 thickness of 96 nm minimizes the reflection. Full three-dimensional modeling yields an optimum thickness of 90 nm, in good agreement with this simplified estimate (see Appendix A for details). We used this 90 nm thickness throughout the optimization leading to the values in Table 2.

Compared to Structure 1, with these SiO_2 and Si_3N_4 ARC layers included in Structure 3, the reflection is suppressed significantly from a maximum value of 27% to a maximum value of 9% for $\lambda_{\text{bg,NWs}} < \lambda < \lambda_{\text{bg,Si}}$ as shown in Fig. 4(a). With these ARCs, the reflection loss for $\lambda < \lambda_{\text{bg,Si}}$ corresponds to a photocurrent density of $j_{\text{R}} = 4.7$ mA/cm² for Structure 1 and $j_{\text{R}} = 1.1$ mA/cm² for Structure 3. Thus, a 77% reduction of the photon loss, in terms of reduction of j_{R} , is achieved by the use of the ARC layers.

To further analyze the anti-reflection effect, we consider the reflection spectrum of Structure 3 with and without these two ARC layers in Fig. 4(b). We see that with a single layer of either SiO_2 or Si_3N_4 , the reflection reduces significantly at the corresponding wavelength of 600 nm and 1000 nm. This reduction shows the validity of our above design. Further analysis can be done with the spectrum-weighted reflection: Without any ARCs, the amount of reflected photons correspond to a photocurrent density of $j_{\text{R}} = 5.9$ mA/cm², as calculated from Eq. (2). After inserting the top side SiO_2 ARC layer, this value goes down to 1.8 mA/cm². Finally, it goes down to the above stated 1.1 mA/cm² by inserting the 90 nm thick Si_3N_4 ARC onto the substrate surface. If only this Si_3N_4 ARC is used, the reflection loss drops from $j_{\text{R}} = 5.8$ mA/cm² to $j_{\text{R}} = 5.3$ mA/cm². Note that the design with only the Si_3N_4 ARC layer present improves only slightly the reflection properties compared to the design without any ARC layers. However, the thickness of this Si_3N_4 layer was fixed to 90 nm, which is optimized for the case of both ARC layers present. Furthermore, the Si_3N_4 layer is placed at the bottom of the nanowire array. Thus, the Si_3N_4 layer is not optimized as a stand-alone ARC layer. Importantly for our purposes, with both ARC layers, the average reflection goes down from 17% to 4% between the bandgap of silicon and the bandgap of the nanowire material.

In the solar spectrum-weighted reflection calculation in Appendix A, we studied the thickness of the Si_3N_4 layer separately from the thickness of the SiO_2 top ARC thickness and the thickness of the ITO layer. The final result of this optimization gives an average of 4% reflection for wavelengths between the bandgap of silicon and the bandgap of the nanowire material.

9. Impact of different models for the absorption in the silicon substrate

Above, we optimized first the absorption of high-energy photons in the nanowires. After that, we discussed the transmission of low-energy photons into the silicon substrate for varying configurations of processing layers. However, the absorption of the transmitted photons depends on the exact geometrical configuration of the silicon substrate. The simplest case is given by assuming full absorption of all photons with $\lambda < \lambda_{\text{bg,Si}}$ that can couple into the silicon [15, 16]. This approximation corresponds to $t_{\text{Si}} \rightarrow \infty$ with t_{Si} the thickness of the silicon substrate or, alternatively, to the use of $X(\lambda) = T(\lambda) = A_{\text{Si}}(\lambda)$ in Eq. (2). We show in Fig. 4(c) (red circles) the results for this approximation for Structure (*) of Table 2.

Alternatively, we could assume a finite thickness for the silicon substrate and use the Beer-Lambert law to calculate a single-pass absorption $A_{\text{Si}}(\lambda) = T(\lambda)[1 - \exp(-\alpha_{\text{Si}}(\lambda)t_{\text{Si}})]$ with $\alpha_{\text{Si}}(\lambda)$ the absorption length in silicon [21]. We show in Fig. 4(c) (green line) results for $t_{\text{Si}} = 300$ μm .

Finally, we include the effect of light trapping due to scattering of light at the top and bottom interface of the silicon substrate more accurately. In the case of $t_{\text{Si}} = 300$ μm , we need to consider that the sunlight [34] loses coherence within the silicon substrate. Therefore, we applied the OPTOS formalism [23] that includes incoherent light propagation within the bulk

of the silicon substrate. However, the diffractive back-scattering from the nanowire array at the top interface was included through the (fully coherent) Maxwell equations [24]. At the bottom interface of the silicon, we placed a diffraction grating in the form of a checkboard pattern of silicon nanosquares on top of a perfect mirror (with $n = 0$ leading to $R = 100\%$). The side length of the squares was $1000/2^{1/2}$ nm, and every second square was raised by 200 nm. This checkboard pattern was rotated by 45° relative to the nanowire array.

The results from this OPTOS calculation of the light-trapping in the silicon substrate, which is textured by the nanowire array at the top interface and the nanosquare grating at the bottom interface, are shown with the magenta line in Fig. 4(c). As expected, these results fall between the results for the approximation of perfect light trapping (as given by $t_{\text{Si}} \rightarrow \infty$) and the approximation of no light trapping (as given by the single-pass absorption for $t_{\text{Si}} = 300 \mu\text{m}$ through the Beer-Lambert law).

Measured EQE of silicon solar cells can show values of 60% and 20% at wavelengths of 1100 and 1150 nm [31]. Comparable values of 55% and 35% were calculated by OPTOS in our designed system at wavelengths of 1100 and 1150 nm. However, the thickness of the silicon cell in our modeling is twice that in the experimental single-junction silicon cell [31], indicating that the light-trapping in the fabricated silicon cell might have been more efficient than in our modeled cell.

In our modeling, for wavelengths below 950 nm, almost all of the light is absorbed before reaching the rear side grating, and all the three above approximations give almost identical results in Fig. 4(c). However, for $\lambda = 1100$ nm, which is very close to the bandgap of 1107 nm of silicon, the $t_{\text{Si}} \rightarrow \infty$ assumption yields $A_{\text{Si}} = 88.7\%$, the OPTOS formalism yields $A_{\text{Si}} = 55.1\%$, and the single-pass absorption yields $A_{\text{Si}} = 8.8\%$. From Eq. (2), we find for these three approximations the respective values of $j_{\text{Si}} = 20.0, 19.1,$ and 16.9 mA/cm^2 for the photocurrent density in the silicon subcell above silicon bandgap of $\lambda_{\text{bg,Si}} = 1107$ nm. Therefore, to optimize the current in the dual junction cell, it is of large importance to consider how the absorption in the silicon cell is modeled. Such considerations become even more important if current matching between the top and the bottom cell is required in a series connected tandem cell, since, as seen above, the estimated photocurrent density in the silicon cell can vary by 15% depending on the approximation. To further illustrate this difference, we calculated the Shockley-Queisser detailed balance efficiency limit from the NW array and Si absorptance curves shown in Fig. 4 (c) [22]. We found that the OPTOS result, where $j_{\text{NWs}} = 21.3 \text{ mA/cm}^2$ and $j_{\text{Si}} = 19.1 \text{ mA/cm}^2$, leads to an efficiency limit of 37.1% for the tandem structure, which is the upper limit for the efficiency potential of our design. By contrast, the single pass approximation, where $j_{\text{NWs}} = 21.3 \text{ mA/cm}^2$ and $j_{\text{Si}} = 16.9 \text{ mA/cm}^2$, gives a 4% lower efficiency limit of 33% in this tandem structure, mainly due to the worse current-matching between the subcells. We recommend to perform an accurate modeling of the light-trapping in the silicon subcell, for example through the OPTOS formalism [23].

Finally, note that in Fig. 4(c), there is noticeably below-bandgap absorption in the OPTOS calculation still at the longest considered wavelength of $\lambda = 1170$ nm, which is beyond $\lambda_{\text{bg,Si}} = 1107$ nm. Such below-bandgap absorption is in line with external quantum efficiency measurements of Si cells, which can typically show short-circuit-current contribution to approximately $\lambda = 1200$ nm [1]. In our case, the absorption in the OPTOS formalism for $1107 \text{ nm} < \lambda < 1200 \text{ nm}$ corresponds to a photocurrent density of 0.6 mA/cm^2 .

10. Conclusion

We considered the absorption of light in a III-V-nanowire-array-on-silicon dual junction solar cell through optical modeling. Specifically, we showed that varying processing layers can have a major impact on the absorption performance of the solar cell. For example, the absorption loss in a 50 nm planar ITO top contact can be 86% lower than in a conformal ITO top contact. Also, we showed the benefit of a design with one ARC at the top of the nanowire array and one ARC on top of the substrate surface. With such ARCs, the reflection loss can

be reduced by 77%. Finally, we showed that different models for the absorption in the silicon substrate can lead to a 15% difference in the estimated photocurrent density in the silicon subcell.

Appendix A: effect of the thickness of the Si₃N₄ ARC

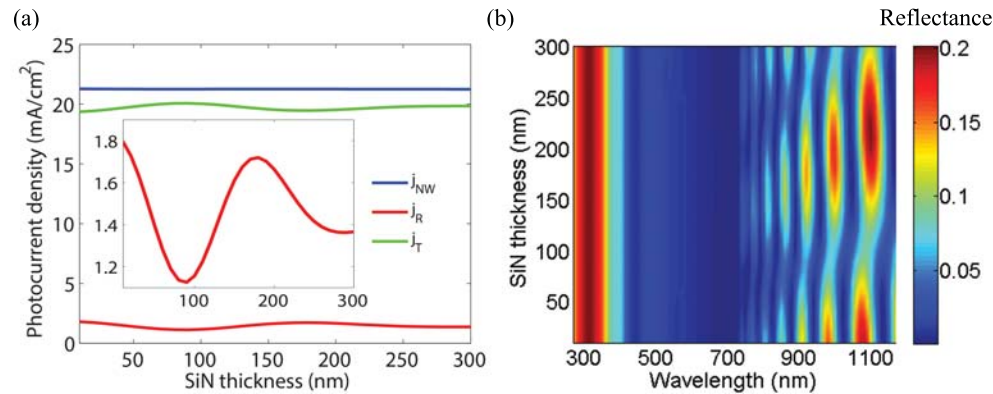


Fig. 5. (a) Reflection, transmission and absorption as a function of Si₃N₄ thickness for the structure marked by (*) in Table 2, translated through Eq. (2) into values equivalent to photocurrent density. The inset shows a zoom-in of the reflection. (b) Corresponding reflectance $R(\lambda)$ for varying Si₃N₄ thickness.

In Fig. 5(a), the reflection, transmission, and absorption are translated into photocurrent density values through Eq. (2). At a thickness of 0 nm for the bottom ARC, the reflection loss corresponds to 1.8 mA/cm². This loss decreases to a minimum value of 1.1 mA/cm² at a thickness of 90 nm. The oscillations in the reflection loss originate from interference effects. Such interference oscillation can be clearly seen in the reflection spectrum as a function of the thickness of the Si₃N₄ in Fig. 5(b).

Appendix B: optimized geometry parameters for nanowire arrays

In the geometry optimization, we categorize the optimum diameter as “HE11” or “HE12”, with the diameter at HE11 smaller than the diameter at HE12. These diameters originate from the HE11 and HE12 absorption resonances in individual nanowires [35], which redshift with increasing diameter. When such a resonance is placed close to the bandgap by tuning the diameter, we can enhance there the absorption in the nanowires, which is otherwise typically weak due to the low absorption coefficient close to the bandgap [36]. By choosing such a diameter and by optimizing at the same time the other geometry parameters, we can optimize the overall absorption of sunlight [22,36]. Note that the HE11 resonance shows typically a stronger absorption than the HE12 resonance.

The surface recombination velocity of InP nanowires can be as low as 170 cm/s [37] while bulk GaP and GaAs can show surface recombination velocity up to 2×10^5 cm/s and 10^7 cm/s, respectively. Therefore, we expect that GaAsP nanowires might show more issues with surface recombination than InGaP nanowires. For this reason, for the GaAsP nanowires that are exposed to air in Structure 1, we included a 10 nm thick $n = 3.5$ radial shell on the GaAsP core of diameter D in order to mimic a high-bandgap III-V semiconductor surface passivation layer. Furthermore, we expect that surface effects, like surface recombination, are decreased relative to bulk effects with increasing diameter since the surface-to-volume ratio decreases. Therefore, for GaAsP, we included in Tables 1 and 2 optimization results both for the smaller-diameter HE11 resonance and the larger-diameter HE12 resonance, even though j_{NWs} is higher for the HE11 resonance.

The geometries shown in Tables 1 and 2 were obtained by optimizing both the nanowire diameter and the array pitch in step of 10 nm [36]. We show examples of such parameter sweeps in Fig. 6 for a few selected systems. In each of Fig. 6(a)-(d), the maximum at the smaller (larger) diameter corresponds to the HE_{11} (HE_{12}) resonance.

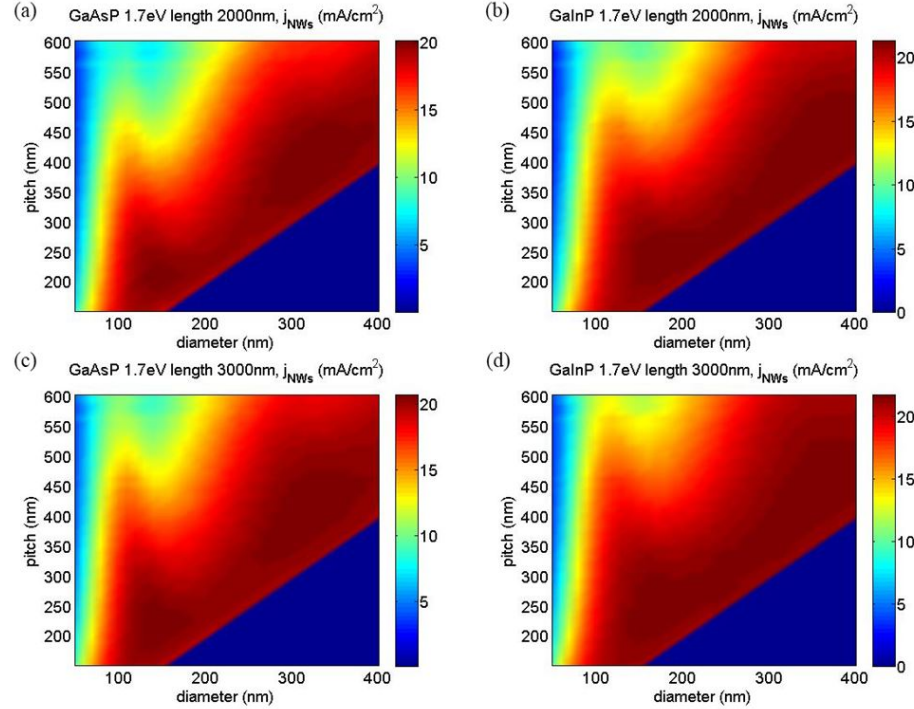


Fig. 6. Photocurrent density j_{NWs} , through Eq. (1), in the nanowire array of Structure 3 (see Fig. 1 for a schematic), as a function of nanowire diameter and array pitch for 2 μm long GaAsP (a) and GaInP (b); and 3 μm long GaAsP (c) and GaInP (d) nanowires.

Table 1. Optimized nanowire diameter D and array pitch P for Structure 1 (see Fig. 1 for a schematic). The values for j_{NWs} , j_T , and j_R are calculated with Eq. (2).

	L (nm)	$E_{bg,NWs}$ (eV)	D (nm)	P (nm)	j_{NWs} (mA/cm ²)	j_T (mA/cm ²)	j_R (mA/cm ²)	j_R for $\lambda_{bg,NWs} < \lambda$ $< \lambda_{bg,Si}$ (mA/cm ²)
GaInP "HE11"	2000	1.64	140	270	22.4	16.7	4.8	3.8
		1.7*	140	260	21.0	17.9	4.9	3.7
		1.74	140	260	20.0	18.8	5.0	3.7
	3000	1.64	150	310	23.1	16.3	4.4	3.6
		1.7	140	290	21.7	17.2	4.8	3.9
		1.74	130	290	20.7	17.8	5.3	4.3
GaAsP "HE11"	2000	1.64	110	250	20.6	18.1	5.1	3.9
		1.7	110	240	19.4	19.2	5.2	3.7
		1.74	110	230	18.0	20.5	5.3	3.5
	3000	1.64	110	270	21.7	17.1	5.0	4.0
		1.7	110	270	20.3	18.2	5.2	4.0
		1.74	110	250	19.0	19.5	5.3	3.8
GaAsP "HE12"	2000	1.64	300	460	20.0	18.0	5.8	3.2
		1.7	280	450	18.7	19.3	5.8	3.4
		1.74	270	450	17.4	20.5	5.9	3.4
	3000	1.64	300	530	20.9	17.5	5.4	3.3
		1.7	280	500	19.6	18.7	5.5	3.4
		1.74	270	500	18.3	19.8	5.7	3.4

Table 2. Optimized nanowire diameter D and array pitch P for Structure 3 (see Fig. 1 for a schematic). The values for j_{NWs} , j_{ITO} , j_{T} , and j_{R} are calculated with Eq. (2).

	L (nm)	$E_{\text{bg,NWs}}$ (eV)	D (nm)	P (nm)	j_{NWs} (mA/cm ²)	j_{T} (mA/cm ²)	j_{R} (mA/cm ²)	j_{R} for $\lambda_{\text{bg,NWs}} < \lambda < \lambda_{\text{bg,Si}}$ (mA/cm ²)	j_{ITO} (mA/cm ²)
GaInP HE11	2000	1.64	190	250	22.7	18.7	1.0	0.6	1.3
		1.7*	170	240	21.3	20.0	1.1	0.8	1.3
		1.74	170	240	20.2	21.1	1.2	0.8	1.3
	3000	1.64	180	260	23.1	18.3	1.1	0.7	1.3
		1.7	180	260	21.7	19.7	1.1	0.7	1.3
		1.74	160	250	20.6	20.6	1.2	0.9	1.4
GaAsP HE11	2000	1.64	150	210	21.4	19.9	1.2	0.7	1.3
		1.7	150	210	20.0	21.3	1.2	0.8	1.3
		1.74	140	200	18.6	22.6	1.3	0.9	1.3
	3000	1.64	150	230	22.1	19.2	1.2	0.8	1.4
		1.7	150	220	20.6	20.6	1.2	0.8	1.4
		1.74	140	210	19.2	22.0	1.3	0.8	1.4
GaAsP HE12	2000	1.64	330	410	21.5	19.9	0.9	0.3	1.4
		1.7	310	400	20.1	21.4	0.9	0.3	1.4
		1.74	300	390	18.7	22.8	0.9	0.4	1.4
	3000	1.64	320	410	22.1	19.4	0.9	0.3	1.4
		1.7	310	400	20.7	10.9	0.9	0.4	1.4
		1.74	300	390	19.3	22.2	0.9	0.4	1.4

Appendix C: ITO absorption loss for larger diameter

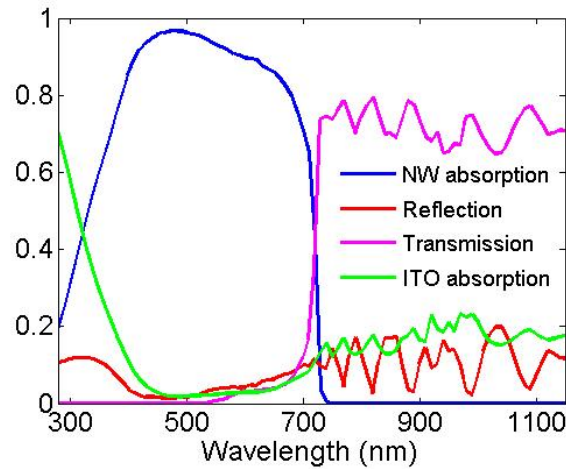


Fig. 7. Structure 2 with GaAsP nanowires of $E_{\text{bg,NWs}} = 1.7$ eV at the larger-diameter HE12 resonance. The ITO thicknesses are indicated in Fig. 1 (b). The geometry parameters are $L = 2000$ nm, $P = 450$ nm and $D = 280$ nm with a 10 nm thick passivation shell of $n = 3.5$, similarly as for the corresponding Structure 1 in Table 1.

As discussed in the main text, the smaller-diameter HE11 resonance showed an ITO absorption corresponding to $j_{\text{ITO}} = 9.4$ mA/cm² for Structure 2 in Fig. 2(a). For that structure, the conformal ITO corresponded to a planar ITO layer of 700 nm in thickness. The larger-diameter HE12 resonance can lead to a smaller amount of ITO. For example, the amount of ITO in the system in Fig. 7 corresponds to a planar thickness of 260 nm. In that case, j_{ITO} decreases to 4.7 mA/cm² as shown in Fig. 7.

Funding

People Programme (Marie Curie Actions) of the European Union's Seventh Framework Programme (FP7-People-2013-ITN) under REA grant agreement No 608153, PhD4Energy, and the European Union's Horizon 2020 Framework Programme under grant agreement No 641023, NanoTandem.

Acknowledgment

This article reflects only the author's view and the Funding Agency is not responsible for any use that may be made of the information it contains. N. Tucher gratefully acknowledges the scholarship support from the Cusanuswerk, Bischöfliche Studienförderung.